

# Detecting charge transfer in defective 2D WS<sub>2</sub> with electron ptychography

Christoph Hofer,<sup>†</sup> Jacob Madson,<sup>‡</sup> Toma Susi,<sup>‡</sup> and Timothy J. Pennycook<sup>\*,†</sup>

<sup>†</sup>*EMAT, University of Antwerp, Belgium*

<sup>‡</sup>*University of Vienna, Faculty of Physics, Boltzmanngasse 5, 1090 Vienna, Austria*

E-mail: [timothy.pennycook@uantwerpen.be](mailto:timothy.pennycook@uantwerpen.be)

## Abstract

Electronic charge transfer at the atomic scale can reveal fundamental information about chemical bonding, but is far more challenging to directly image than the atomic structure. Bonding generally involves a relatively small perturbation of the total charge density dominated by the atomic nuclei, and thus detecting any change due to bonding requires a higher level of sensitivity than structural imaging. Here we apply the dose efficiency of electron ptychography to detect charge transfer in both the pristine structure of monolayer WS<sub>2</sub> and at its defects, even at modest electron irradiation doses. Ptychography allows residual aberrations that effect the phase images to be corrected after collection, leading to excellent agreement with first-principles image simulations including where thermal diffuse scattering is explicitly modeled via finite-temperature molecular dynamics based on density functional theory. The focused-probe ptychography configuration also provides the important ability to concurrently collect the annular dark-field signal, which allows unambiguous interpretation of the atomic structure and chemical identity of the atoms, independently of the charge transfer. Our results demonstrate both the power of ptychographic reconstructions and the importance of quantitatively accurate simulations to aid their interpretation.

## Introduction

Chemical bonding is what makes an ensemble of independent atoms into a material with collective properties. As a central tenet of density functional theory (DFT),<sup>1,2</sup> these materials properties can be entirely derived from the electron charge density. As such, measuring the charge density experimentally is of great interest. Electron diffraction and X-ray scattering are both capable of detecting the influence of charge transfer,<sup>3-6</sup> but both methods generally probe an average over a large area rather than individual atoms or atomic columns. For imaging atomic structures, electron microscopy has become an indispensable tool, and in recent years, scanning transmission electron microscopy (STEM) the de facto standard due to the simplicity of interpreting atomic-number contrast with its annular dark-field (ADF) modality.<sup>7</sup> However, that method is not sensitive to the electron charge distribution, as its contrast results from Rutherford scattering from the nuclear cores. The inelastic scattering processes detected by electron energy loss spectroscopy (EELS) do contain information about the local environment,<sup>8,9</sup> but require high electron irradiation doses for a signal that is sufficient for spectral analysis as well as the use of demanding first-principles spectrum simulations to interpret its fine structure.<sup>8</sup>

Phase contrast imaging methods, on the other hand, are known for being highly dose efficient, and indeed local atomic-scale detection of charge redistribution due to bonding has been demonstrated in high-resolution transmission electron microscopy (HRTEM) for both single-layer boron nitride and doped graphene.<sup>10</sup> This involved performing image simulations using potentials that included bonding via DFT calculations as well as potentials produced from an independent atom model (IAM),<sup>11</sup> in which individual non-interacting atomic potentials are simply superimposed to create the total potential and thus electron redistribution due to the interaction of atoms is not taken into account. However, revealing the charge redistribution in HRTEM required the careful use of specific contrast transfer function (CTF) conditions using large defocus values, to the detriment of image resolution as the charge transfer signal is usually hidden in low-frequency contribution of the image.

Furthermore, it can be challenging to ensure that the aberrations used to set up a given CTF are correct. This of course is in addition to the fact that the complexity of the HRTEM CTF generally tends to make image interpretation difficult even for atomic structure determination, let alone teasing out the electron redistribution due to bonding from the same signal, without a simultaneously available reference of the structure itself.

Fortunately, STEM phase-imaging techniques have advanced greatly over the past decade and are now capable of providing highly dose-efficient images that are sensitive to the total projected potential, including redistribution due to bonding. Many of these techniques can further be performed with an atomically focused probe, and can be acquired simultaneously with ADF images that are predominantly sensitive to the nuclear potentials and thus the atomic structure alone. For example, differential phase contrast (DPC) and scattering center-of-mass (CoM)-based images are related to the total charge density of the imaged material.<sup>12-14</sup> Moreover, 4D-STEM, in which the detailed scattering distribution is recorded as a 2D image at each probe position of the 2D scan, enables higher-accuracy CoM measurements compared to using a few-segment DPC detector. Importantly, 4D-STEM also enables us to perform electron ptychography, which brings significantly higher dose efficiency compared to both HRTEM<sup>15</sup> and CoM-based imaging<sup>16,17</sup> as well as the ability to correct residual aberrations,<sup>18</sup> which could otherwise cause an incorrect measurement of the charge density. We use these capabilities to experimentally visualize charge transfer in monolayer WS<sub>2</sub>.

Enhanced dose efficiency is important because the amount of charge transferred in bonding is very small compared to the total charge density, making it challenging to detect, particularly when the sample can be damaged by the electron beam itself. For example, defects in 2D materials are known to be highly mobile under the electron beam, generally ruling out the use of high electron doses.<sup>19,20</sup> However, simple sample drift from slow imaging can also greatly impede image interpretation, particularly when attempting to detect changes in charge as small as the redistribution of individual electrons. To enable fast data acquisition, we use an event-driven camera, allowing us to capture 4D datasets at fast ADF

imaging speeds (MHz).<sup>21</sup> We use these to average drift-corrected frames where the structure has not been altered.<sup>20</sup> The simultaneously acquired ADF image is used for  $Z$ -contrast imaging, while the reconstructed phase image facilitates visualizing light elements as well as measuring the charge redistribution. We use focused-probe single side band (SSB) ptychography<sup>22</sup> as our reconstruction algorithm to calculate the phase contrast. Two convergence semiangles, 20 and 30 mrad, are used, and the aberrations of each dataset evaluated and corrected post-acquisition.<sup>18</sup> We use this method to analyse charge transfer in pristine as well as in defective WS<sub>2</sub> as representative of 2D transition metal dichalcogenides (TMDs).

The results are interpreted in light of multislice simulations based on an all-electron electrostatic potential calculated with density functional theory (DFT). Experimental parameters are reproduced in the simulation of 4D data sets, which are then reconstructed using the same SSB algorithm in an all-Python workflow. To correctly include the effect of thermal diffuse scattering when charge transfer is important, we use DFT-based molecular dynamics to generate explicit molecular dynamics (MD) frozen-phonon snapshots, which further improves the agreement with the experiment.

## Results and discussion

Although state-of-the-art aberration correctors can largely eliminate the effects of phase aberrations, the correction is never perfect and slight lens instabilities can also introduce residual aberrations without visually obvious changes in the final image but which can nevertheless impact an analysis of the subtle effect of charge transfer. Contrast change induced by aberrations is problematic when quantifying the phase or intensity of the atoms,<sup>23,24</sup> as well as for analysing charge distribution.<sup>25</sup> Post-acquisition aberration correction in electron ptychography is therefore importantly able to negate the influence of such residual aberrations in the phase images. This is illustrated in the experimental data of WS<sub>2</sub> in Fig. 1. The SSB image in panel b relies solely on the hardware aberration corrector for correcting

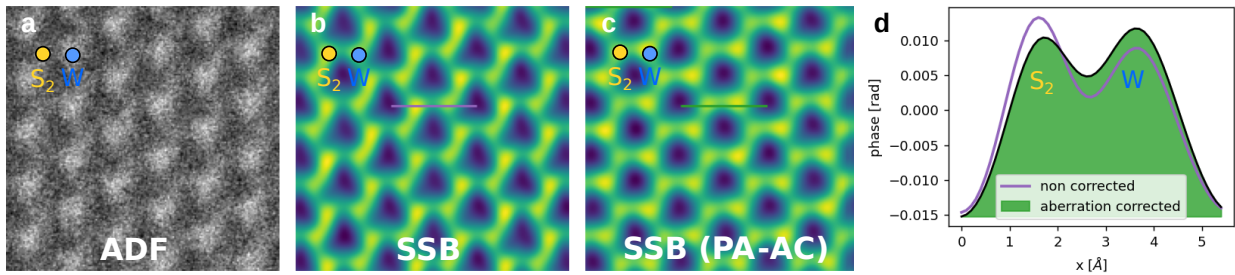


Figure 1: **Post-collection aberration corrected single side band (SSB) reconstruction.** a) Low-dose ADF image of  $WS_2$ . b) SSB reconstruction of the same scan with slight residual aberrations. c) Aberration-corrected SSB reconstruction. d) Line profile showing a reversal of the sublattice contrast between b and c.

probe aberrations before acquisition. The atoms are clearly resolved and rotationally symmetric and the residual aberrations calculated using ptychography are relatively small (see Supplement). However the phase is higher for the  $S_2$  sites than the  $W$  sites as seen in the line profile in panel d. The post-acquisition corrected image in panel c, however, shows a higher contrast for the  $W$  site for these specific imaging parameters, which as we will show later, agrees with the results of DFT. Importantly, the simultaneously acquired ADF image immediately allows us to assign the correct element to each sublattice.

To understand the role of charge transfer in producing the observed contrast, we turn to first-principles calculations and SSB ptychography image simulations based on DFT and IAM potentials. 4D-STEM convergent-beam electron diffraction (CBED) data sets were simulated using the multislice algorithm with the *abTEM* code,<sup>26</sup> with the probe parameters and sampling matching our experimental condition (see Methods), and then used for ptychographic reconstructions using the same SSB algorithm as for the experimental data. As we will discuss later, the resulting contrast between the sublattice sites depends on the convergence angle of the incoming probe. For the 20 mrad convergence angle used in Fig. 1, the IAM-based  $S_2$  phases are higher than those of  $W$  sites. However, once bonding is included by using a potential based on DFT, the contrast reverses, with the  $W$  sites having higher phase than the  $S_2$  sites. This is exactly what is seen in Fig. 1c once post-collection

aberration correction is applied to the ptychographic image. This makes physical sense from the electronegativity of the elements: S has a higher electronegativity than W, resulting in a calculated charge transfer of 1.36 electrons from the W to the neighboring S (see Methods), leading to increased screening and therefore a smaller phase shift of the  $S_2$  sites.

To quantify the influence of the charge redistribution from the ptychographic images, we need to assign a phase to each of the atomic sites. Various approaches have been established for quantifying the atomic intensities of ADF images, including local maxima,<sup>7</sup> the integration of Voronoi cells,<sup>27</sup> Gaussian fits,<sup>28,29</sup> as well as template matching.<sup>24</sup> These methods can in principle also be used for phase images. Simple use of local maxima are generally problematic for low-dose scans due to the poor robustness of the method with respect to noise. For methods such as Voronoi tessellation, the ptychographically reconstructed images generally have to be renormalized as they typically oscillate around zero which cancels out when integrating to obtain a total quantitative phase value for an atomic site. Voronoi tessellation after squaring the phase image has been used to handle these negative values,<sup>30</sup> but this is not ideal for defects as the squared phase over-emphasises the centers of the hexagons compared to the atomic sites themselves where vacancies appear. We propose that rigidly shifting the phases such that the center of the hexagons is set to zero could be a better solution than using the squared phase.

Here, however, we instead use an optimization method where the convolution of a probe and a 2D model of point phase objects is matched to the target image via iterative optimization of the model and optionally the probe shape.<sup>24</sup> The probe is chosen to match the contrast transfer function of SSB.<sup>31</sup> (A detailed description of the method is beyond this work and will be published in a separate article.) This method turns out to be more robust to sample tilt, which is crucial to obtain a good match between the simulation and experiment. The cost-function that is minimized is the negative correlation between the convolved image and the target image. The target can be either an experimental image or the result of simulations, allowing us to compare the quantitative atomic intensities from the model values

for our experiments and simulations based on both DFT and IAM potentials. Importantly, we again emphasise that because we perform SSB using focused-probe data, we are able to independently determine the identity of the atomic sites from the simultaneously acquired ADF images and distinguish between W and S<sub>2</sub> sites, which is not always straightforward from phase-data alone, especially when it is potentially aberrated.

## Pristine WS<sub>2</sub>

Fig. 2 compares pristine WS<sub>2</sub> SSB data from experiments and simulations based on IAM and DFT potentials. Line profiles taken across the W and S<sub>2</sub> sites for the simulations are displayed in panel b. Including bonding via DFT clearly alters the relative phases of the two sublattices. The ratio of the phases of the sites depends on the convergence angle as shown in panel d. This is no surprise as the convergence angle will determine the strength at which different spatial frequencies are transferred in the SSB method,<sup>16,31</sup> which in turn determines the relative strengths at which the features of the charge density distribution appear in the phase images. However, the fact that we can see these clear differences does demonstrate that the frequencies transferred by these conditions do contain information on the charge transfer induced by bonding. We emphasize that such conditions are all in the range typical for normal high-resolution STEM imaging. This is in contrast to using conventional HRTEM, where the imaging conditions relevant to detecting the charge transfer are often not those desired for imaging the structure itself.

For each convergence angle, the phase ratio of the S<sub>2</sub> to the W sites is lower when bonding is included. This is, again, expected from the increased screening from the charge transfer involved in bonding, and indeed is a far better match to what we see experimentally. The quantified atomic phases from our experiments were classified according to their lattice site, facilitated by the ADF signal, allowing us to determine the mean phase of each atomic site. This is shown in histogram form in Fig. 2c for the 20 mrad experimental data shown in panel a. For each data set, we carefully selected contamination-free areas which resulted in a total

number of approximately 15 sites analysed.

Including atomic vibrations using thermal diffuse scattering (TDS) slightly decreases the ratio of the two types of sites compared to neglecting it, and the experimental error bar contains both values. The experimental error estimated by the statistical atom-by-atom phase variation is dominated by the limited signal, which can be reduced by increasing the number of atomic sites sampled. In the present case, the number was limited by carefully excluding any areas with indications of surface contamination, as this would distort the measured phases, and to a lesser degree by the multiframe alignment and averaging. The TDS analysis in Fig. 2d used the relatively low dose of  $1 \times 10^5 e^-/\text{\AA}^2$ , which gives a similar error bar to the experimental value as the limited signal is the main contribution to the limited precision. Crucial for a good match between experiment and DFT simulation is the optimization method as it takes into account the effect of sample tilt.

## Defective $\text{WS}_2$

The simplest defect in TMDs is a chalcogen vacancy. For  $\text{WS}_2$  this can be realized by knocking out a single S atom, leaving behind a S vacancy and a remaining S atom at the former  $\text{S}_2$  site. This produces a significantly reduced phase in SSB reconstructions, as shown in the DFT-based SSB images in Fig 3a and c. This data also showcases the ability of ptychography to reveal light atoms next to heavy elements<sup>17,18</sup> as the S vacancy is only discernible in the phase image and not the ADF image (see Supplement Fig. 1). Interestingly, we observe a higher W phase close to S vacancies in both experiments and DFT simulations, with the intensity of the W depending on the density of the vacancies in the area. The reason for this is two-fold: firstly, the CTF of the SSB reconstruction results in a negative beam tail that reduces the phase contrast of atoms close to other ones. Importantly, the phase quantification method we use is taking this into account, allowing us to detect the second effect, the charge transfer from the S vacancy to the W itself.

To study this phenomena theoretically, we simulated a small region of  $\text{WS}_2$  introducing

one, two and three S vacancies. Fig. 3a and b show the DFT phase images of one and three vacancies, respectively, where the W phase is clearly visually higher in the latter case. The difference between IAM- and DFT-based potentials is also increasing at the W site next to the defects. The charge transfer from the S vacancies to the specific W atom ranges from  $0.20\text{ }e^-$  for a single vacancy to  $0.55\text{ }e^-$  for the triple vacancy, as estimated using Bader analysis (see Methods). This is demonstrated in Fig. 3e, where the green dashed circles indicate the S vacancy (single S) sites. Interestingly, this transfer of electrons to the W site is the opposite of what happens in the pristine structure, where W transfers electrons to the neighbouring S sites. The change in charge at the S sites is negligible, since three

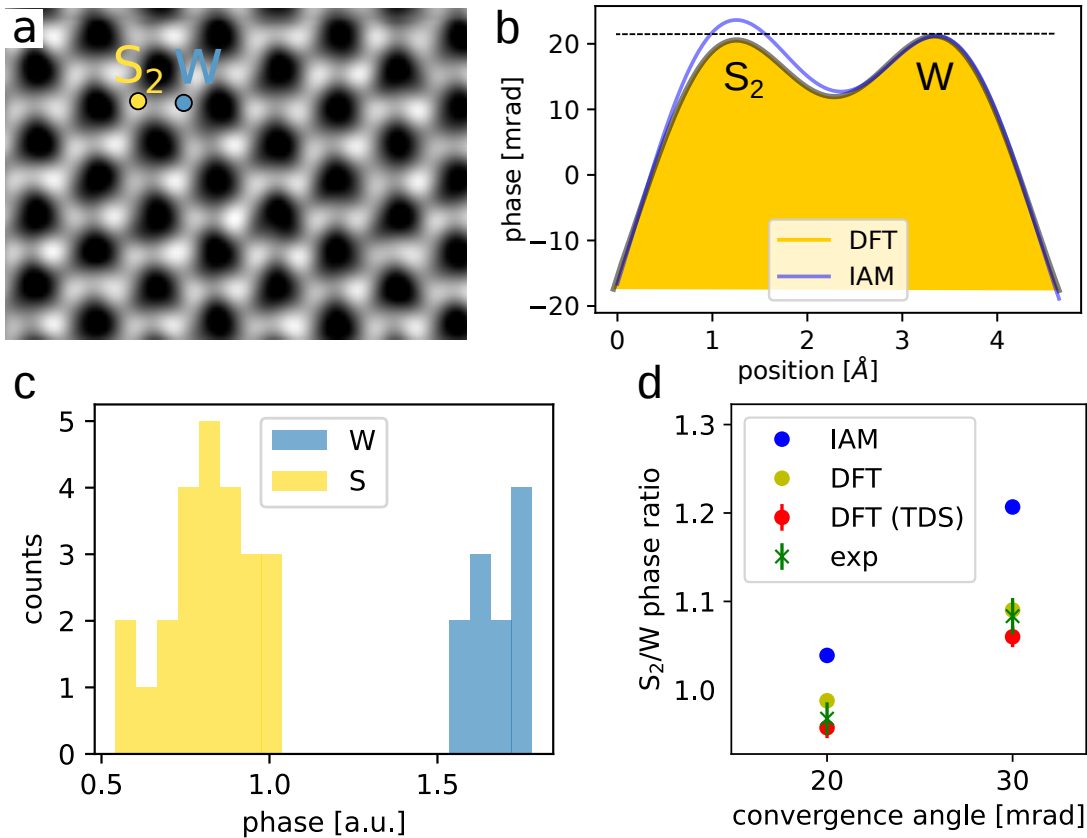


Figure 2: **Charge-transfer measurement in  $\text{WS}_2$ .** a) Experimental SSB image using a convergence angle of 20 mrad. b) Comparison of line profiles of SSB simulations using DFT and IAM potentials. c) Histogram of the phases from the two sublattices in the 20 mrad experimental SSB image. d) Ratio of the mean values of the two sublattices as a function of convergence angle using IAM and DFT potentials with and without the effect of TDS, compared with experimental data for 20 and 30 mrad.

S atoms share the 0.55 electrons. Indeed, this charge transfer also directly effects the SSB phase-contrast image, where a difference of approx. 4% can be detected. The difference increases with a higher density of defects (see Fig. 3b and d), making the charge transfer easier to detect in highly defected areas (see Supplement).

To observe these phenomena experimentally, we introduced defects, including such vacancies, into  $\text{WS}_2$  using the electron beam. Indeed, a large area scan shows a high variation of the phase and a significant overlap in the histogram (see Supplement). A representative defective area is shown in Fig. 3f, where the S vacancies are indicated by the green circles. As one can see, the W intensities are significantly higher within the highly defected area.

To quantify the effect of charge transfer in these defects, we simulated a highly defected area with a similar configuration as observed experimentally and compared the ratio between the S vacancy and the neighbouring W. Indeed, the best match of the simulation is obtained when thermal vibrations as well as charge transfer is included in the simulations ( $W/S_{vac} = 2.05$ ) and the poorest match is obtained when using the IAM-based simulation ( $W/S_{vac} = 1.90$ ). However, the ratio is still higher in the experimental case ( $W/S_{vac} = 2.24 \pm 0.09$ ). To reduce the uncertainty estimate, we performed this analysis on a large area to obtain a sample of 26 vacancy configurations. Since each configuration is differently influenced by neighboring defects, a variation of the phase beyond noise is unavoidable and this mismatch of 10% might be due to a higher defect density in the experiment than in the simulations.

## Conclusions

We have experimentally detected charge transfer in monolayer  $\text{WS}_2$  by electron ptychography, including at vacancy defects. This is made possible by the influence of the electron distribution in the material on the electron phase. The benefit of post-collection aberration correction is crucial to obtain accurate phases for charge-transfer measurements. We have also shown that the convergence angle is an important parameter when imaging the charge transfer, as it defines which frequencies are transferred in the phase images. Our results in-

dicate that the frequencies at which charge transfer is detectable conveniently include those used for atomic-resolution imaging. The simulations based on first-principles charge redistribution and thermal vibrations lead to an excellent agreement in the pristine case. For defective areas, we observe a notable phase increase of the metal site close to chalcogen vacancy sites due to both the contrast transfer function of the single side band reconstruction and the charge transfer.

## Methods

### Sample preparation

WS<sub>2</sub> was synthesized on Si/SiO<sub>2</sub> by physical vapor deposition from WS<sub>2</sub> powder. The flakes were then transferred to a Quantifoil(R) TEM grid by a drop of isopropanol. The transfer was completed by etching the SiO<sub>2</sub> with a KOH solution and cleaning by deionized water.

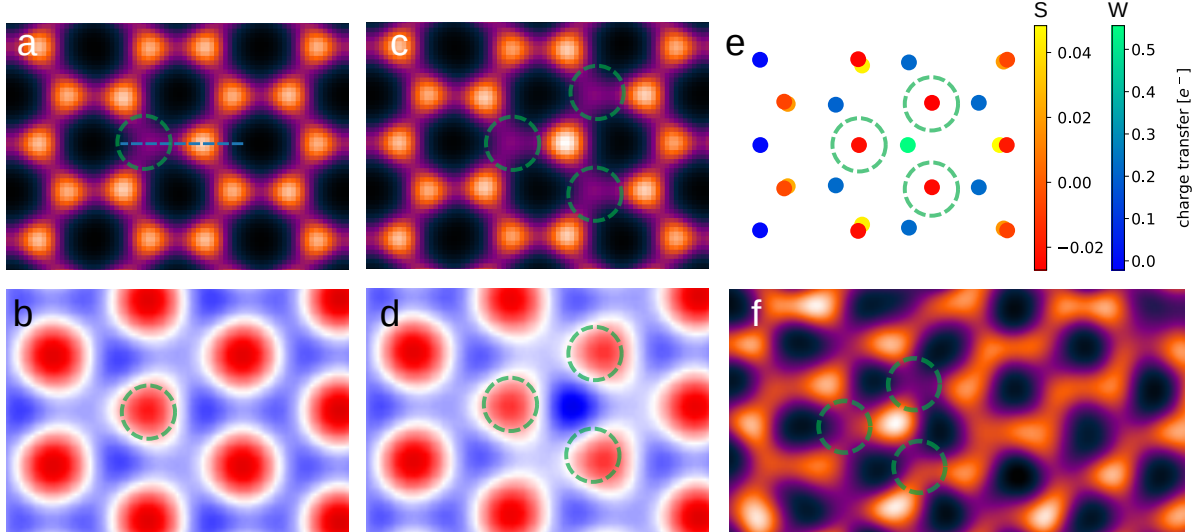


Figure 3: **Analysis of defective WS<sub>2</sub>.** SSB simulation of a single S vacancy (a) and three S vacancies (c). Difference between IAM and DFT simulations of a single vacancy (b) and three S vacancies (d). (e) Charge transfer of three S vacancies to the central W. (f) Experimental SSB image of defective WS<sub>2</sub> showing higher W intensities close to S vacancies (green circles).

## Transmission electron microscopy

STEM experiments at 60 kV were conducted by a ThermoFisher Themis Z instrument equipped with a Timepix3 camera. The probe convergence angle was set to 20 and 30 mrad and the beam current was ca. 2 pA. Typical 4D data sets included  $1024 \times 1024$  probe positions with a dwell time of 1–5  $\mu$ s. The list of events provided by the Timepix3 was reconverted to a 4D data set using an in-house code.

The detector sampling was chosen to be approx. 30–40 pixels for the bright field disk and the real-space sampling was ca. 0.1–0.15  $\text{\AA}$  per pixel. The ADF detector semi-angular range was 70 to 220 mrad. To increase the signal-to-noise ratio, several frames (up to 10) were aligned and averaged. Typical resulting total doses were approx.  $10^5 e^-/\text{\AA}^2$ .

## Density functional theory

For DFT, we used the projector-augmented wave method in the open-source package GPAW.<sup>32</sup> The minimal hexagonal unit cell of WS<sub>2</sub> was made orthogonal, its size was optimized, and then used to create  $5 \times 3 \times 1$  supercells of WS<sub>2</sub> (a total of 90 atoms) with a minimum of 8.9  $\text{\AA}$  of vacuum between the periodic images of the layers (perpendicular cell size of 12  $\text{\AA}$ ).

To obtain relaxed structures for the multislice simulations, the atomic positions were optimized using a plane-wave basis with a cutoff energy of 500 eV and  $3 \times 3 \times 1$   $\mathbf{k}$ -points to sample the Brilloin zone until residual forces on the atoms were below 0.02 eV/ $\text{\AA}$ . To create models with defects, we removed one or more S atoms, and re-relaxed the atomic positions.

## Charge transfer

Charge transfer between the W and S<sub>2</sub> columns was estimated via Bader partitioning<sup>33</sup> of the charge density using the grid-based implementation of Henkelman and colleagues.<sup>34</sup> The resulting atomic charges for the pristine system were compared to those calculated for atoms surrounding the S vacancy.

## Multislice simulations

For the multislice simulations, the DFT potential was calculated from the all-electron charge density converged with GPAW, as described previously.<sup>35</sup> For the IAM, the potential was taken to be a superposition of individual tabulated atomic potentials, as parametrized by Lobato.<sup>36</sup> A lateral real-space sampling of 0.05 Å has been used for both potentials as well as a perpendicular slice thickness of 1.0 Å.

Thermal diffuse scattering was included by running DFT-based velocity-Verlet molecular dynamics (MD) with time step of 2 fs, initialized with a Maxwell-Boltzmann temperature of 300 K and thermalized for 100 time steps. Ten MD frozen-phonon snapshots were generated by saving the converged electron density every 50 time steps, and data sets averaged over the ensemble.

4D-STEM simulations were carried out using the multislice approach as implemented in the open-source package *abTEM*.<sup>26</sup> All simulation parameters were set to the experimental parameters, including the convergence angles and the dose per area (simulated as Poisson noise). The reciprocal-space sampling was 0.06 Å<sup>-1</sup>. For ADF, we note that DFT and IAM models produce essentially identical contrast.

## Single side band ptychography

SSB ptychography was performed with the open-source PyPtychoSTEM package,<sup>37</sup> using either the experimental or simulated 4D-STEM data sets as input. The step size was chosen to be 0.15 Å per pixel and the voltage was 60 kV. The convergence angle was set to 20 mrad or 30 mrad.

## References

- (1) Hohenberg, P.; Kohn, W. Inhomogeneous Electron Gas. *Phys. Rev.* **1964**, *136*, B864–B871.

(2) Kohn, W.; Sham, L. J. Self-Consistent Equations Including Exchange and Correlation Effects. *Phys. Rev.* **1965**, *140*, A1133–A1138.

(3) Coppens, P.; Stevens, E. D. In *Accurate X-Ray Diffraction and Quantum Chemistry: The Study of Charge Density Distributions*; Löwdin, P.-O., Ed.; Advances in Quantum Chemistry; Academic Press, 1977; Vol. 10; pp 1–35.

(4) Koritsanszky, T. S.; Coppens, P. Chemical Applications of X-ray Charge-Density Analysis. *Chemical Reviews* **2001**, *101*, 1583–1628, PMID: 11709993.

(5) Zuo, J. M. Measurements of electron densities in solids: a real-space view of electronic structure and bonding in inorganic crystals. *Reports on Progress in Physics* **2004**, *67*, 2053–2103.

(6) Wu, L.; Zhu, Y.; Tafto, J. Test of first-principle calculations of charge transfer and electron-hole distribution in oxide superconductors by precise measurements of structure factors. *Phys. Rev. B* **1999**, *59*, 6035–6038.

(7) Krivanek, O. L.; Chisholm, M. F.; Nicolosi, V.; Pennycook, T. J.; Corbin, G. J.; Dellby, N.; Murfitt, M. F.; Own, C. S.; Szilagyi, Z. S.; Oxley, M. P.; Pantelides, S. T.; Pennycook, S. J. Atom-by-atom structural and chemical analysis by annular dark-field electron microscopy. *Nature* **2010**, *464*, 571–574.

(8) Ramasse, Q. M.; Seabourne, C. R.; Kepaptsoglou, D.-M.; Zan, R.; Bangert, U.; Scott, A. J. Probing the Bonding and Electronic Structure of Single Atom Dopants in Graphene with Electron Energy Loss Spectroscopy. *Nano Letters* **2013**, *13*, 4989–4995, PMID: 23259533.

(9) Tan, H.; Turner, S.; Yücelen, E.; Verbeeck, J.; Van Tendeloo, G. 2D Atomic Mapping of Oxidation States in Transition Metal Oxides by Scanning Transmission Electron Microscopy and Electron Energy-Loss Spectroscopy. *Phys. Rev. Lett.* **2011**, *107*, 107602.

(10) Meyer, J. C.; Kurasch, S.; Park, H. J.; Skakalova, V.; Künzel, D.; Gross, A.; Chuvalin, A.; Algara-Siller, G.; Roth, S.; Iwasaki, T.; Starke, U.; Smet, J. H.; Kaiser, U. Experimental analysis of charge redistribution due to chemical bonding by high-resolution transmission electron microscopy. *Nature materials* **2011**, *10*, 209–215.

(11) Kirkland, E. J. Advanced Computing in Electron Microscopy. 1998.

(12) Gao, W. et al. Real-space charge-density imaging with sub-ångstrom resolution by four-dimensional electron microscopy. *Nature* **2019**, *575*, 1–1.

(13) Gao, W. et al. Real-space charge-density imaging with sub-ångstrom resolution by four-dimensional electron microscopy. *Nature* **2019**, *575*, 1–1.

(14) Calderon V, S.; Ferreira, R. V.; Taneja, D.; Jayanth, R.; Zhou, L.; Ribeiro, R. M.; Akinwande, D.; Ferreira, P. J. Atomic Electrostatic Maps of Point Defects in MoS2. *Nano Letters* **2021**, *21*, 10157–10164, PMID: 34846155.

(15) Pennycook, T. J.; Martinez, G. T.; Nellist, P. D.; Meyer, J. C. High dose efficiency atomic resolution imaging via electron ptychography. *Ultramicroscopy* **2019**, *196*, 131–135.

(16) O’Leary, C. M.; Martinez, G. T.; Liberti, E.; Humphry, M. J.; Kirkland, A. I.; Nellist, P. D. Contrast transfer and noise considerations in focused-probe electron ptychography. *Ultramicroscopy* **2021**, *221*, 113189.

(17) Gao, C.; Hofer, C.; Jannis, D.; Béché, A.; Verbeeck, J.; Pennycook, T. J. Overcoming contrast reversals in focused probe ptychography of thick materials: An optimal pipeline for efficiently determining local atomic structure in materials science. *Applied Physics Letters* **2022**, *121*, 081906.

(18) Yang, H.; Rutte, R.; Jones, L.; Simson, M.; Sagawa, R.; Ryll, H.; Huth, M.; Pennycook, T.; Green, M.; Soltau, H.; Kondo, Y.; Davis, B.; Nellist, P. Simultaneous atomic-

resolution electron ptychography and Z-contrast imaging of light and heavy elements in complex nanostructures. *Nature Communications* **2016**, *7*, 12532.

(19) Sun, L.; Banhart, F.; Warner, J. Two-dimensional materials under electron irradiation. *MRS Bulletin* **2015**, *40*, 29–37.

(20) de Graaf, S.; Kooi, B. J. Radiation damage and defect dynamics in 2D WS2: a low-voltage scanning transmission electron microscopy study. *2D Materials* **2021**, *9*, 015009.

(21) Jannis, D.; Hofer, C.; Gao, C.; Xie, X.; Béché, A.; Pennycook, T.; Verbeeck, J. Event driven 4D STEM acquisition with a Timepix3 detector: Microsecond dwell time and faster scans for high precision and low dose applications. *Ultramicroscopy* **2022**, *233*, 113423.

(22) Pennycook, T. J.; Lupini, A. R.; Yang, H.; Murfitt, M. F.; Jones, L.; Nellist, P. D. Efficient phase contrast imaging in STEM using a pixelated detector. Part 1: Experimental demonstration at atomic resolution. *Ultramicroscopy* **2015**, *151*, 160–167, Special Issue: 80th Birthday of Harald Rose; PICO 2015 – Third Conference on Frontiers of Aberration Corrected Electron Microscopy.

(23) Lehtinen, O.; Geiger, D.; Lee, Z.; Whitwick, M. B.; Chen, M.-W.; Kis, A.; Kaiser, U. Numerical correction of anti-symmetric aberrations in single HRTEM images of weakly scattering 2D-objects. *Ultramicroscopy* **2015**, *151*, 130 – 135, Cited by: 10; All Open Access, Green Open Access.

(24) Hofer, C.; Skákalová, V.; Haas, J.; Wang, X.; Braun, K.; Pennington, R. S.; Meyer, J. C. Atom-by-atom chemical identification from scanning transmission electron microscopy images in presence of noise and residual aberrations. *Ultramicroscopy* **2021**, *227*, 113292.

(25) Martis, J. et al. Imaging the electron charge density in monolayer MoS2 at the Ångstrom scale. 2022; <https://arxiv.org/abs/2210.09478>.

(26) Madsen, J.; Susi, T. The abTEM code: transmission electron microscopy from first principles [version 2; peer review: 2 approved]. *Open Research Europe* **2021**, *1*.

(27) E, H.; MacArthur, K.; Pennycook, T.; Okunishi, E.; D'Alfonso, A.; Lugg, N.; Allen, L.; Nellist, P. Probe integrated scattering cross sections in the analysis of atomic resolution HAADF STEM images. *Ultramicroscopy* **2013**, *133*, 109 – 119, Cited by: 103.

(28) Van Aert, S.; Verbeeck, J.; Erni, R.; Bals, S.; Luysberg, M.; Dyck, D. V.; Tendeloo, G. V. Quantitative atomic resolution mapping using high-angle annular dark field scanning transmission electron microscopy. *Ultramicroscopy* **2009**, *109*, 1236 – 1244, Cited by: 166.

(29) De Backer, A.; van den Bos, K.; Van den Broek, W.; Sijbers, J.; Van Aert, S. StatSTEM: An efficient approach for accurate and precise model-based quantification of atomic resolution electron microscopy images. *Ultramicroscopy* **2016**, *171*, 104 – 116, Cited by: 114; All Open Access, Green Open Access.

(30) O'Leary, C. M.; Haas, B.; Koch, C. T.; Nellist, P. D.; Jones, L. Increasing Spatial Fidelity and SNR of 4D-STEM Using Multi-Frame Data Fusion. *Microscopy and Microanalysis* **2022**, *28*, 1417–1427.

(31) Yang, H.; Pennycook, T. J.; Nellist, P. D. Efficient phase contrast imaging in STEM using a pixelated detector. Part II: Optimisation of imaging conditions. *Ultramicroscopy* **2015**, *151*, 232–239, Special Issue: 80th Birthday of Harald Rose; PICO 2015 – Third Conference on Frontiers of Aberration Corrected Electron Microscopy.

(32) Enkovaara, J. et al. Electronic Structure Calculations with GPAW: A Real-Space Implementation of the Projector Augmented-Wave Method. *J. Phys. Condens. Matter* **2010**, *22*, 253202.

(33) Bader, R. *Atoms in Molecules: A Quantum Theory*; Oxford University Press, 1990.

(34) Tang, W.; Sanville, E.; Henkelman, G. A Grid-Based Bader Analysis Algorithm without Lattice Bias. *J. Phys.: Condens. Matter* **2009**, *21*, 084204.

(35) Susi, T.; Madsen, J.; Ludacka, U.; Mortensen, J. J.; Pennycook, T. J.; Lee, Z.; Kotakoski, J.; Kaiser, U.; Meyer, J. C. Efficient First Principles Simulation of Electron Scattering Factors for Transmission Electron Microscopy. *Ultramicroscopy* **2019**, *197*, 16–22.

(36) Lobato, I.; Van Dyck, D. An Accurate Parameterization for Scattering Factors, Electron Densities and Electrostatic Potentials for Neutral Atoms That Obey All Physical Constraints. *Acta Crystallographica Section A* **2014**, *70*, 636–649.

(37) C. Hofer, T. P., C. Gao PyPtychoSTEM. <https://gitlab.com/pyptychostem/pyptychostem>, 2021.

## Acknowledgement

We acknowledge funding from the European Research Council (ERC) under the European Union’s Horizon 2020 Research and Innovation Programme via Grant Agreement No. 802123-HDEM (C.H. and T.J.P.) and Grant agreement No. 756277-ATMEN (J.M. and T.S), and FWO Project G013122N “Advancing 4D STEM for atomic scale structure property correlation in 2D materials” (C.H.). We gratefully acknowledge computational resources provided by the Vienna Scientific Cluster (VSC).

## Supporting Information Available

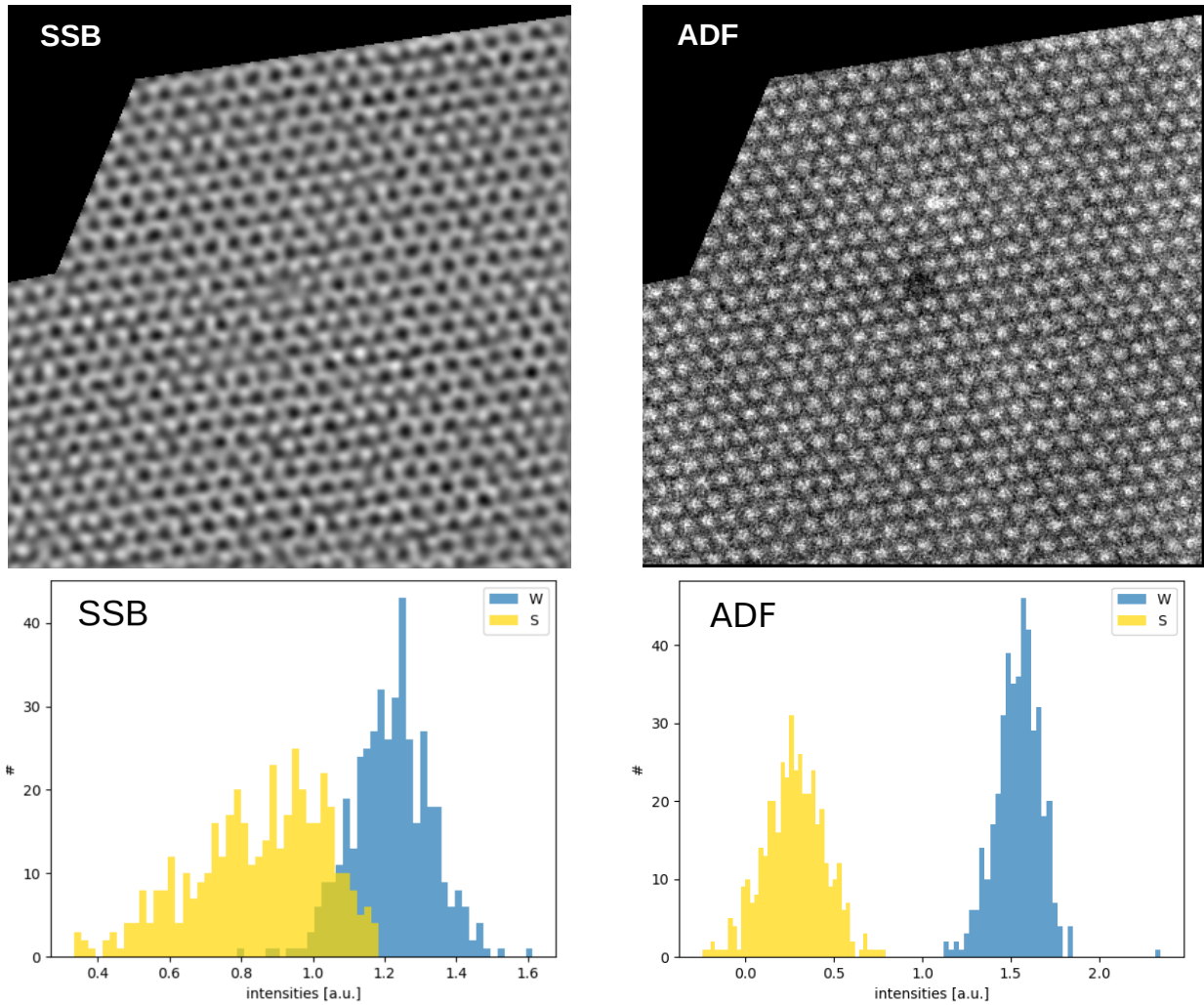
### Complete area of defective $WS_2$

SFig. 1 shows a larger area of defective  $WS_2$ . The sublattices can be easily distinguished by the high W intensity in the ADF image on the right, whereas the S site and their vacancies cannot be distinguished. The SSB image, however, gives a good contrast between S and their vacancies. The charge-transfer dependence on defect density gives a large variation of phases in the corresponding histograms.

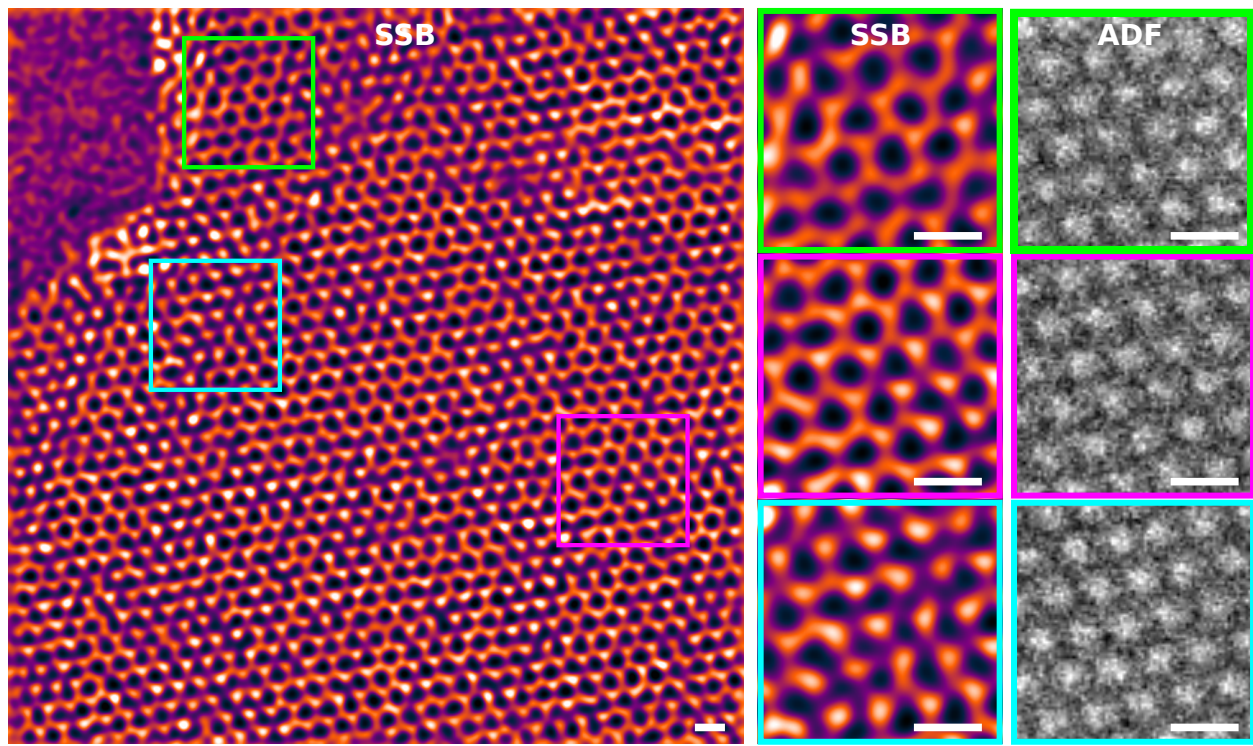
SFig. 2 shows different areas. The green box shows a small region of pristine lattice, the purple box a region with several S vacancies, and the cyan box shows a full line defect.

SFig. 3 an experimental SSB image of a defective region. All phases are extracted and shown in the corresponding histograms to the right. For this specific region, the assignment of S vacancies, the pristine sites (S and W) and the W close to the S vacancies ( $W@S_{vac}$ ) are done manually. As one can see, the  $W@S_{vac}$  sites are the highest. The experimental ratio between  $W@S_{vac}$  and  $S_{vac}$  has the best match with the DFT-TDS simulations, despite of a small residual mismatch.

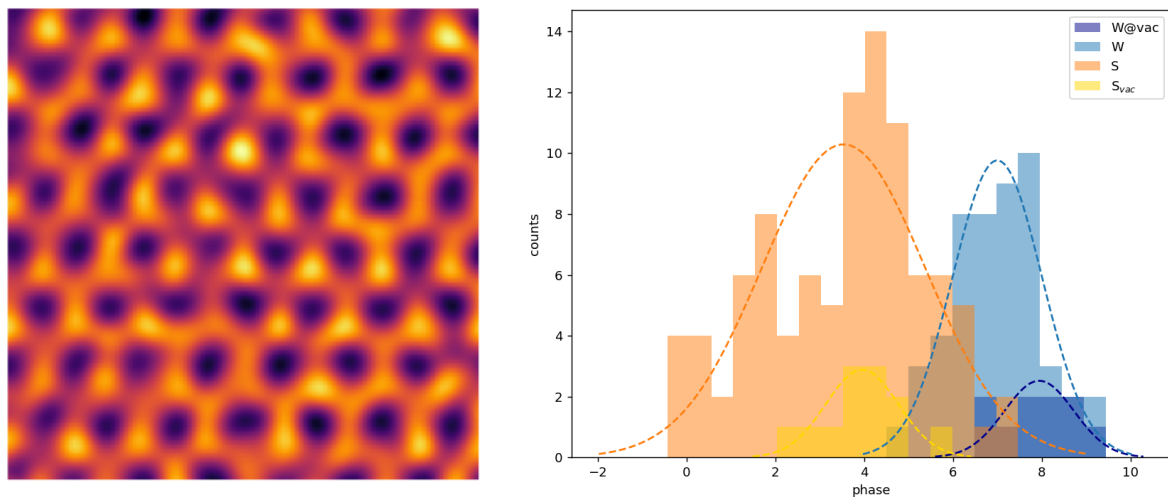
SFig. 4 analyses the W phase next to vacancies as a function of the number of S vacancies. It shows the absolute (blue) and relative (orange) differences between the IAM- and DFT-based SSB image, revealing that the relative difference is higher when the number of vacancies are higher. This is due to a lower charge transfer from the W vacancies to S as there are less S atoms compared to the pristine case.



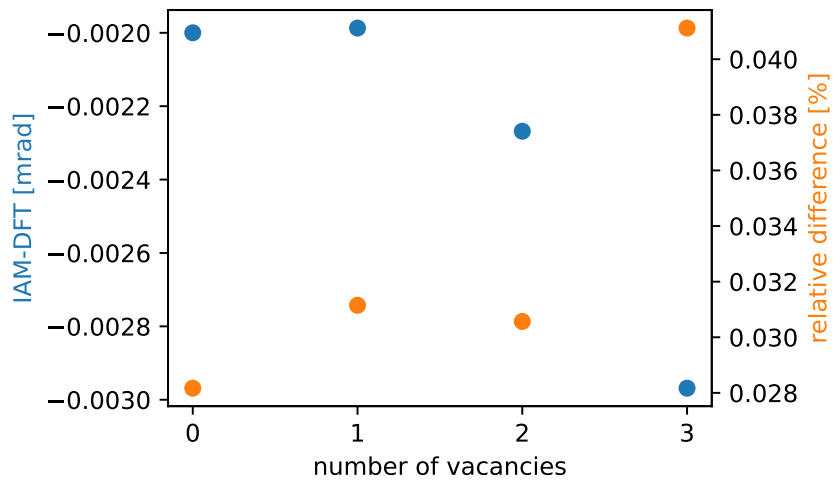
Supplementary Figure 1: **Histogram of phases.** Top: SSB and ADF image of a defective area. Bottom: Histogram of extracted phases for both sites, W and S.



Supplementary Figure 2: Regions with different defect densities.



Supplementary Figure 3: Analysis of phase cross section at defective area. Left: Experimental SSB image of a small defective area. Right: Analysis of defect sites.



Supplementary Figure 4: **Analysis of phase charge transfer measurement of different density of defects.** Absolute and relative difference between IAM and DFT based SSB phase reconstruction of a W atom next to the vacancies.